

Commissioning of a multi-beamline femtoslicing facility at SOLEIL

Marie Labat,^{a,*} Jean-Blaise Brubach,^a Alessandra Ciavardini,^a Marie-Emmanuelle Couprie,^a Erik Elkaim,^a Pierre Fertey,^a Tom Ferte,^d Philippe Hollander,^a Nicolas Hubert,^a Emmanuelle Jal,^e Claire Laulhé,^{a,b} Jan Luning,^{a,e} Olivier Marcouillé,^a Thierry Moreno,^a Paul Morin,^a Francois Polack,^a Pascale Prigent,^a Sylvain Ravy,^c Jean-Paul Ricaud,^a Pascale Roy,^a Mathieu Silly,^a Fausto Sirotti,^a Amina Taleb,^a Marie-Agnès Tordeux^a and Amor Nadjji^a

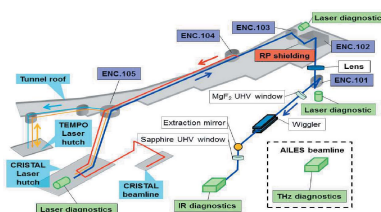
^aSynchrotron SOLEIL, Saint-Aubin, 91191 Gif-sur-Yvette, France, ^bUniversité Paris-Saclay, Université Paris-Sud, F-91405 Orsay Cedex, France, ^cLaboratoire de Physique des Solides, Université Paris-Sud, F-91405 Orsay Cedex, France, ^dUniversité de Strasbourg, CNRS, Institut de Physique et Chimie des Matériaux de Strasbourg, UMR 7504, F-67000 Strasbourg, France, and ^eSorbonne Universités, UPMC Université Paris 06, CNRS, Laboratoire de Chimie Physique – Matière et Rayonnement, 75005 Paris, France. *Correspondence e-mail: marie.labat@synchrotron-soleil.fr

The investigation of ultrafast dynamics, taking place on the few to sub-picosecond time scale, is today a very active research area pursued in a variety of scientific domains. With the recent advent of X-ray free-electron lasers (XFELs), providing very intense X-ray pulses of duration as short as a few femtoseconds, this research field has gained further momentum. As a consequence, the demand for access strongly exceeds the capacity of the very few XFEL facilities existing worldwide. This situation motivates the development of alternative sub-picosecond pulsed X-ray sources among which femtoslicing facilities at synchrotron radiation storage rings are standing out due to their tunability over an extended photon energy range and their high stability. Following the success of the femtoslicing installations at ALS, BESSY-II, SLS and UVSOR, SOLEIL decided to implement a femtoslicing facility. Several challenges were faced, including operation at the highest electron beam energy ever, and achievement of slice separation exclusively with the natural dispersion function of the storage ring. SOLEIL's setup also enables, for the first time, delivering sub-picosecond pulses simultaneously to several beamlines. This last feature enlarges the experimental capabilities of the facility, which covers the soft and hard X-ray photon energy range. In this paper, the commissioning of this original femtoslicing facility is reported. Furthermore, it is shown that the slicing-induced THz signal can be used to derive a quantitative estimate for the degree of energy exchange between the femtosecond infrared laser pulse and the circulating electron bunch.

1. Introduction

Sub-picosecond X-ray pulses have become an essential tool for the investigation of ultrafast dynamics, for example for studying chemical reactions and ultrafast phase transitions. Provided by free-electron lasers (FELs) in the hard as well as in the soft X-ray range (Ackermann *et al.*, 2007; Shintake *et al.*, 2008; Emma *et al.*, 2010; Ishikawa *et al.*, 2012; Allaria *et al.*, 2012), but with a limited capacity, such pulses are also in demand at synchrotron facilities which remain more easily accessible.

As the electron beam dynamics in storage rings naturally maintains the pulse duration above a few tens of picoseconds, several methods have been proposed to overcome this limitation. SOLEIL took its first step towards pulse length



reduction providing a two-week per year low- α operation (Tordeux *et al.*, 2012), where the whole machine optics is modified to lower the momentum compaction factor. To also provide sub-picosecond X-ray pulses to its user community, the femtoslicing technique (Zholents & Zolotarev, 1996) has been chosen, leaving out other schemes such as crab cavities (Zholents *et al.*, 1999), coherent harmonic generation (Prazeres *et al.*, 1988) or echo-enabled harmonic generation (Evain *et al.*, 2012).

A femtoslicing experiment requires a relativistic electron beam and a laser pulse of short duration (a few tens of femtoseconds), propagating in the same direction inside a wiggler used as modulator. When the electron beam passes through the magnetic field of the modulator, it wiggles with the same period as the magnetic field period λ_w and produces synchrotron radiation at the resonant wavelength $\lambda_R = (\lambda_w/2\gamma^2)(1 + K^2/2)$. γ is the Lorentz factor of the electron beam and K is the modulator deflection parameter which can be tuned by the modulator gap. If the laser wavelength λ_L satisfies the resonance condition $\lambda_L = \lambda_R$, overlapping the laser electric field onto the electron beam inside the wiggler leads to an energy exchange. The electron beam energy distribution becomes longitudinally modulated over the interaction region, *i.e.* over a ‘slice’ roughly as short as the laser pulse duration ΔT_{Laser} . The energy modulation is characterized by a periodicity λ_L and an amplitude ΔE . When the slice of energy-modulated electrons propagates through a dispersive element such as a bending magnet, it splits transversely into two sub-slices since half of the modulated electrons experienced a positive energy gain and the other half a negative energy gain. Each of these slices then radiates a sub-picosecond synchrotron radiation pulse at downstream beamline source points. Radiation from the beam core is blocked with slits, the positions of which impact the intensity as well as the signal-to-background ratio of the femto-pulse. Owing to the dispersion properties of the ring, the local energy modification introduced in the interaction region is rapidly converted into a typically 1 mm-long density depletion. Passing through magnetic dipoles, this depleted or ‘holed’ electron bunch produces a coherent THz signal directly correlated to the efficiency of the energy exchange and thus can be used for diagnostic purposes (Holldack *et al.*, 2006).

Since its proposal in 1996, femtoslicing experiments have been successfully implemented on four machines. In 2000, the Advanced Light Source (ALS, USA) reported a proof-of-principle experiment (Schoenlein *et al.*, 2000). Operating the storage ring at 1.5 GeV, the level of energy exchange was estimated *via* the measurement of the FEL gain while dipole synchrotron radiation pulses of 300 fs FWHM duration were observed. A few years later, BESSY-II (Germany) successfully commissioned, with an electron beam at 1.7 GeV, the first undulator-based femtoslicing beamline (Holldack *et al.*, 2005). Its angular slice separation scheme relied on a closed-orbit bump using three dipoles while the THz signal induced by the energy modulation was used to optimize the interaction. Further measurements demonstrated the broadband emission characteristics of the THz radiation pulses, an emission

content which also enabled one to estimate that the THz pulse duration was in the sub-picosecond range (Holldack *et al.*, 2006). The femtoslicing installation at the Swiss Light Source (SLS), operated on a 2.41 GeV electron beam, is also based on an undulator, which radiates in the hard X-ray photon energy range and thus enables the investigation of laser-driven structural dynamics (Beaud *et al.*, 2007). The THz signal was used to optimize the interaction. While previous experiments targeted sub-picosecond pulses delivery in the X-ray range, the experiments performed on the UVSOR storage ring, operated at 0.6 GeV, are dedicated to THz radiation applications (Shimada *et al.*, 2007). Following the predictions of an analytical model, several innovative machine studies were achieved to show the spectral narrowing and tunability possibilities, as well as laser power scalings, of such laser-induced coherent THz sources (Bielawski *et al.*, 2008; Evain *et al.*, 2010; Hosaka *et al.*, 2013).

Benefiting from all those experiences, SOLEIL intended to challenge the present femtoslicing experiments limits and to demonstrate, and operate, a new configuration (Nadji *et al.*, 2004). The achievement of a satisfying energy exchange level had to meet four major challenges. Besides using an electron beam at higher energy than elsewhere together with a wiggler designed as both a modulator and a synchrotron radiation source for users, the natural dispersion function had to be elegantly used for the slice separation and this slice was to be used simultaneously on several beamlines.

One key parameter of a femtoslicing experiment is the electron energy modulation amplitude ΔE which must exceed the natural energy spread σ_E of the electron beam by a factor of ~ 5 for an efficient use of the femtoslice (Zholents & Zolotarev, 1996). As the laser pulse energy required scales as ΔE^2 and as storage rings are usually designed to ensure $\sigma_E \simeq 0.001E$, it becomes clear that the required laser energy roughly scales as E^2 . SOLEIL chose to operate the femtoslicing experiments at its nominal 2.75 GeV energy and therefore ranks as the most demanding machine in terms of laser energy.

The use of a single wiggler (Marcouillé *et al.*, 2014) as both a modulator for the femtoslicing experiments and, alternately, as a hard X-ray synchrotron radiation source for the PUMA beamline (<https://www.synchrotron-soleil.fr/fr/lignes-de-lumiere/puma>) was a non-negligible aspect of the project challenges. It required indeed an optimization of the magnetic field at two different gaps [one targeting a resonance wavelength in the infrared (IR) range for the femtoslicing and the other targeting a broad hard X-ray and high-power spectral content for the PUMA beamline].

Previous installations systematically added a horizontal dispersion bump after the interaction section by means of three additional bending magnets, to separate the slices from the core beam. SOLEIL only uses the natural dispersion function of the machine without any change in the storage ring optics.

Finally, the number of beamlines involved in a femtoslicing project is limited by the natural stretching of the slice along the non-isochronous ring, consequently limiting the number of femtoslicing users. At SOLEIL, for the first time, two beam-

lines are already simultaneously benefiting from sub-picosecond pulses and at least two other beamlines could be added.

In this paper we report on the commissioning of this original femtoslicing setup and the present status of double user operation. In particular, we present a detailed analysis of the THz signals that derive from the femtoslicing, an analysis which provides an estimate of the absolute energy exchange level reached at SOLEIL.

2. Experimental setup

2.1. General layout

The femtoslicing setup (Labat *et al.*, 2014; Prigent *et al.*, 2014) is illustrated in Fig. 1. The experiment stretches across all the synchrotron building, *i.e.* over more than 150 m, involving equipment placed at three beamlines (CRISTAL, TEMPO and AILES), two laser hutches and inside the ring tunnel.

The main IR femtoslicing laser is installed in a hutch near the CRISTAL beamline (<http://www.synchrotron-soleil.fr/Recherche/LignesLumiere/CRISTAL>; Laulhé *et al.*, 2012, 2013). The full laser power is transported over 100 m (blue line in Fig. 1) out of the laser hutch through a viewport and up to the tunnel roof to the enclosure labeled ENC.104. At this stage the beam is split into two branches using a standard beamsplitter.

The main power is transmitted straight forward over the tunnel roof, then down inside the tunnel through a dedicated shielding (ENC.102), before reaching the final focusing lens and an entrance MgF₂ viewport for injection in the vacuum chamber of the storage ring. The laser beam then propagates freely along the wiggler, where it interacts with the electron beam. The wiggler was designed for both the femtoslicing project and the hard X-ray beamline PUMA. The gap can be remotely adjusted to vary the resonant wavelength λ_R . Typical gaps for femtoslicing operation, *i.e.* resonance setting around 800 nm, are in the 17 mm range. Closing the gap down to 14.5 mm will allow the PUMA beamline to work with hard X-ray photons with energies spanning the range 10–70 keV.

In parallel, the low laser power branch generated by the beamsplitter is sent back to the experimental hutch of the CRISTAL beamline (red line in Fig. 1). The beamsplitter location is chosen so as to equalize the times of flight down to the sample in the CRISTAL beamline of the pump branch (red line in Fig. 1) and of the femtosecond X-ray probe branch resulting from the laser/electron interaction. Note that in this experimental scheme one single laser pulse is used to create the IR pump and the X-ray probe, which ensures by design a sufficient level of synchronization between the two pulses.

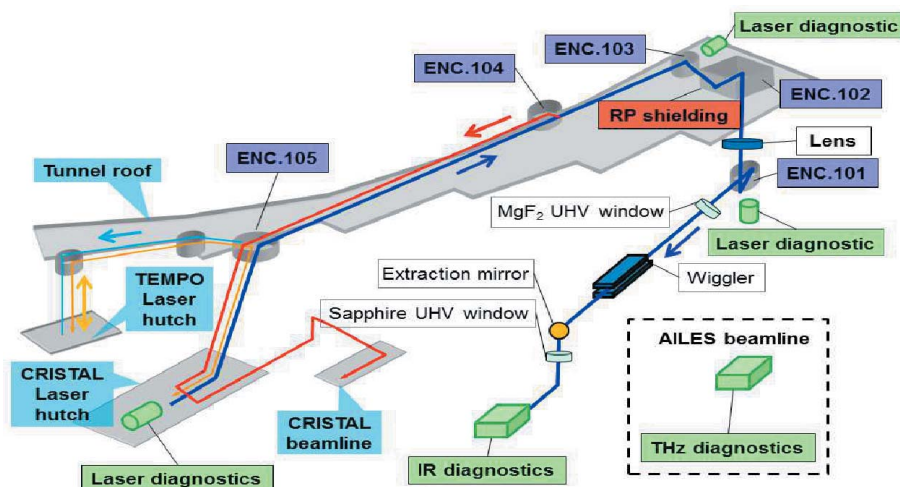


Figure 1

Overview of the femtoslicing facility at SOLEIL. ENC.: enclosure (vacuum chamber). Dark blue line: femtoslicing laser path from the CRISTAL laser hutch to the modulator (wiggler). In ENC.104, a beamsplitter sends back 10% of the laser power to the CRISTAL beamline (red line). Cyan and orange lines: laser paths to the TEMPO beamline. The AILES beamline and associated THz diagnostics are presented in an inset as are located out of the scale of this drawing.

Another transport line has been installed between the main laser hutch and the TEMPO beamline (<http://www.synchrotron-soleil.fr/Recherche/LignesLumiere/TEMPO>; Silly *et al.*, 2017). This line can be either used to synchronize the TEMPO laser with the main laser (orange line in Fig. 1), or for the direct pumping of samples during femtosecond pump-probe experiments on the TEMPO beamline (cyan line in Fig. 1).

Femtosing is now operated during normal user operation in the hybrid mode. The sliced bunch is an isolated single bunch of 5 mA which lies at the center of an empty ring quarter. It is characterized by a typical energy spread σ_e above 0.1% and a bunch length σ_z of about 30 ps RMS. The remaining three quarters are uniformly filled with 312 lower-intensity bunches (1.5 mA), which brings the total current stored to 450 mA (Nadolski *et al.*, 2014).

2.2. Laser transport

The main femtoslicing laser is a Ti:Sa laser from Coherent (Legend Elite Duo-USX) with a central wavelength at $\lambda_L = 800$ nm and a bandwidth of $\Delta\lambda_L \simeq 60$ nm FWHM. The amplifier can deliver pulses of up to 5 mJ at a repetition rate of 1 kHz with a minimum pulse duration of $\Delta T_{\text{Laser}} = 25$ fs FWHM.

Since the laser had to be transported and aligned over ~ 100 m, special care was taken in the design and implementation of the optical enclosures and transport diagnostics (grey and green cylinders, respectively, in Fig. 1). They consist of near- and far-field imaging systems (Prigent *et al.*, 2014) using leaks behind the strategic transport mirrors. A first pair of mirrors inside the laser hutch is used to align the beam from the laser hutch up to the last mirror on the tunnel roof (MIR.104) located in enclosure ENC.103. The laser position is

accurately adjusted using a near-field diagnostic behind MIR.104. The mirror MIR.104 is then used to adjust roughly the laser position and angle throughout the wiggler using the near- and far-field diagnostics located behind the last injection mirror, MIR.101, located under ENC.101.

In order to maximize the interaction in the wiggler, the laser must be focused inside the wiggler (Zholents & Holldack, 2006). The laser waist size is adjusted using a pair of lenses (one focusing and one defocusing) inside the laser hutch together with a single focusing lens (9 m focal length) inside the tunnel. Varying the distance between the first pair of lenses enables the beam waist size to be tuned together with the waist position inside the wiggler, however not independently. This variable will be referred to in the following as $f\#$, which ranges between 1 and 5 in arbitrary units, 1 corresponding to the shortest and 5 to the longest distance between the lenses.

The laser propagation throughout the whole transport line was modelled using the optical design software *Zemax* (<http://www.zemax.com/os/opticstudio>), including the transport mirrors, the shaping lenses, but also the inner vacuum chamber geometry. Fig. 2(a) shows that the calculated waist size varies within the 200–500 μm range while tuning $f\#$ in the 1–5 range, and Fig. 2(b) shows the drift of the calculated waist position *versus* $f\#$. The calculated waist position is found to be in good

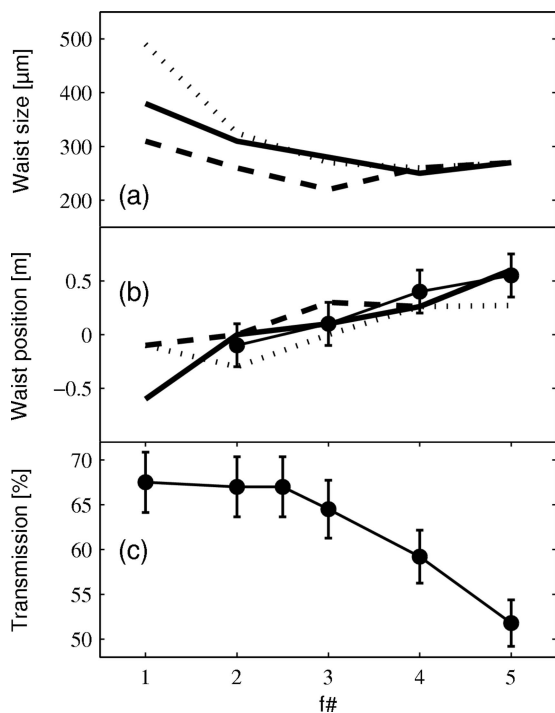


Figure 2 Laser transport properties *versus* focusing setting $f\#$ in arbitrary units. (a) Laser waist size calculated at 760 nm (dashed line), 800 nm (full line) and 840 nm (dotted line) with *ZEMAX* assuming a time-diffraction limited Gaussian beam. (b) Laser waist position relative to the wiggler center calculated with *ZEMAX* assuming a time-diffraction limited Gaussian beam [same line styles as for (a)] and (black circles) measured removing the wiggler vacuum chamber and using a laser power of 0.6 W with a pulse duration of 4 ps FWHM. (c) Laser power transmission from the laser amplifier output to the wiggler entrance, measured as in (b). Error bars on the black circles correspond to the precision of the measurements.

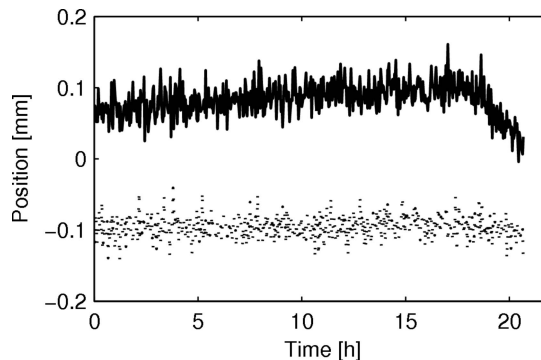


Figure 3 Laser pointing stability without feedback measured on the diagnostic below ENC.101 (near-field imaging on a CCD camera). Full line: horizontal plane. Dashed line: vertical plane.

agreement with the measurements performed inside the wiggler.

As illustrated in Fig. 2(c), the tuning of the laser waist also has a dramatic impact on the final power transmission to the wiggler. For tighter focusings (higher $f\#$) inside the wiggler, the beam is larger at upstream locations where the inner diameter of the vacuum chambers is critical, causing higher transmission losses. In addition, whatever $f\#$, the transmission remains below 68%. This is due to the high number of optics on the laser path (more than ten mirrors, one beamsplitter, three lenses and two windows). The laser power inside the wiggler could only be measured once, since this requires dismantling the vacuum chamber of the wiggler. This is why, in the following, we preferred to indicate the laser power P_{Laser} measured before transport to characterize our experimental conditions.

The final $f\#$ operating point is around 2. This results from a compromise between centering the waist position inside the wiggler and maximizing the transmitted power to maximize the interaction level, and limiting the waist size, *i.e.* power density, not to break the window ensuring the air-to-vacuum transition.

The first long sessions of user operation allowed us to study the laser pointing stability at the entrance of the wiggler using the diagnostics installed below ENC.101 (see Fig. 1). As presented in Fig. 3, the drift of the transverse positions of the laser beam does not exceed 0.2 mm, which corresponds to pointing drifts lower than 40 μrad within 20 h. The observed drifts are essentially due to the environment (slow variations of the hall temperature and humidity). A feedback control of the pointing is currently being implemented in order to suppress those slow drifts. Fast variations of the laser beam positions are also observed, corresponding to the intrinsic pointing fluctuations of the laser ($\pm 15 \mu\text{rad}$).

2.3. IR diagnostics

The infrared diagnostics used for the spatial, spectral and temporal alignments of the laser on the electron beam in the interaction region are located at the wiggler exit, inside the tunnel (Labat *et al.*, 2014). A removable copper mirror can be

inserted in order to collect the 800 nm radiation out of the wiggler (synchrotron radiation and femtosecond laser radiation). A camera (scA640 from Basler) and a set of plano-convex lenses allows imaging inside the wiggler to achieve the spatial alignment, a spectrometer (UBS2000 from Ocean Optics) is used to check the spectral overlap while a fast diode (FPD 310-FV from Menlo) enables adjusting the synchronization of the laser with the electron beam on a time scale of a few picoseconds.

Since the copper mirror can only sustain synchrotron radiation powers from maximum ring currents of 5 mA (100 W at 5 mA), the infrared diagnostics are blind in user operation mode. In fact, even in the alignment phase with a ring current below 5 mA, some thermal effects appeared after a few hours of operation: the high-power synchrotron radiation of the wiggler distorted the imaging of the beams inside the wiggler. Performing alignment with ring currents below 1 mA was the only way to limit the aberrations.

2.4. THz diagnostics

In femtoslicing operation, coherent THz radiation is emitted at each dipole of the ring. Nevertheless, efficient THz radiation collection is only achieved at the AILES beamline (<https://www.synchrotron-soleil.fr/fr/lignes-de-lumiere/ailles>; Dalla Bernardina *et al.*, 2014), dedicated to IR absorption spectroscopy for materials and molecules. This is the reason why the THz diagnostics for the femtoslicing project were installed on the AILES beamline (low-resolution branch), located 298 m downstream of the interaction point.

The exact transmission of the AILES beamline is not accurately known. Nevertheless, we can reasonably assume, given the design of the whole beamline (Brubach *et al.*, 2010), that the theoretical bending-magnet radiation spectrum (see the dashed line in Fig. 4) is transmitted with a constant attenuation from 0.2 up to 3 THz. Frequencies below 0.2 THz are cut by the accelerator vacuum chamber.

Three different diagnostics have been used for the femtoslicing commissioning: a bolometer (InSb Hot Electron Bolometer from IR-Labs), a fast diode (12C-LS2500 from

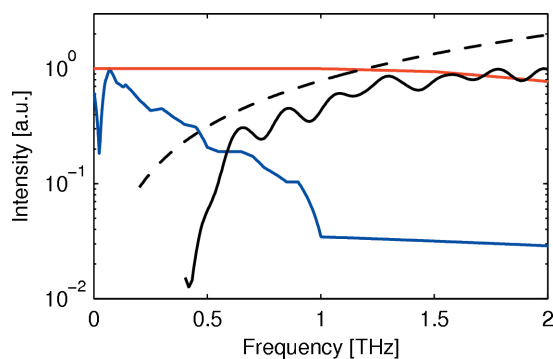


Figure 4 Dashed line: theoretical incoherent synchrotron radiation spectrum expected on the AILES beamline without femtoslicing. Spectral normalized response of (black line) the low-resolution branch spectrometer, (blue line) the diode and (red line) the bolometer. Responses measured in the case of the spectrometer, theoretical in the case of the diode and of the bolometer.

Table 1 Parameters for the simulation of the interaction.

Parameter	Unit	Value
Beam energy	MeV	2739
Horizontal beam size [†]	μm RMS	200
Vertical beam size [†]	μm RMS	20
Beam relative energy spread	–	0.001016
Bunch duration at 5 mA	ps RMS	30
Modulator period λ_w	mm	164
Modulator number of periods N_w	–	20
Laser central wavelength	nm	800
Laser bandwidth	nm FWHM	60
Laser repetition rate	kHz	1
Laser pulse maximum energy	mJ	5
Laser pulse minimum duration	fs FWHM	25

[†] In the middle of the wiggler.

ACST) and a spectrometer (iFS125HR from Bruker). These detectors were alternatively installed depending on the required type of measurement.

Because of its high sensitivity, the bolometer was used as the main diagnostic in the commissioning phase. As shown in Fig. 4, its theoretical spectral response is nearly constant over our range of interest (0.2–2 THz). In addition, its sub-microsecond response time enables the turn-by-turn signal to be resolved.

The diode has a lower sensitivity but a faster response time (1 ns) than the bolometer and, whereas the bolometer needs periodic manual liquid-helium refilling of its cooling system, the diode is operated in a standalone mode at room temperature. This second detector was therefore used for monitoring purposes during long-term (typically one week) femtoslicing experiments. The diode theoretical spectral response falls smoothly from 0.2 to 2 THz (see Fig. 4).

Both detectors (bolometer and diode) can be saturated in femtoslicing operation at currents above a few milli-amperes. In this case we attenuate the incident radiation by inserting into the beam a thick fused silica filter (favouring low frequencies) and/or metallic grid filters (favouring high frequencies).

The spectrometer was only used in dedicated sessions to investigate the spectral content of the THz radiation. Fig. 4 shows that the spectrometer is blind below 0.4 THz because of its 6 μm mylar beamsplitter used for the interferometric process. The ripples in the spectrum are due to Fabry–Perot effects inside this same beamsplitter. Since the acquisition time is typically of a few seconds, unlike the bolometer and the diode, the spectrometer does not resolve the turn-by-turn signal: all turn contributions are mixed.

3. Femtoslicing modelling

3.1. Energy exchange in the wiggler

The energy exchange in the wiggler is simulated using two different codes: *GENESIS* (Reiche, 1999) and *ELEGANT* (Borland, 2000). In both cases, the electron beam is defined according to the parameters given in Table 1. A six-dimensional Gaussian distribution ($x, x', y, y', t, \delta E/E$) is created using RMS parameters. Here, (x, y, x', y') are the transverse

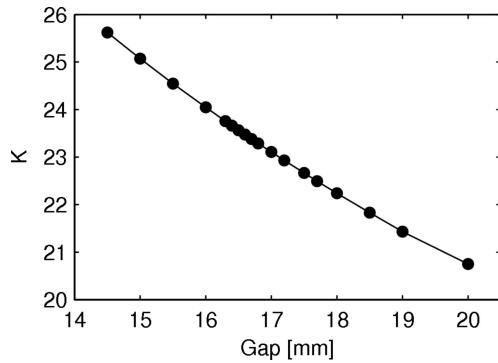


Figure 5
Deflection parameter K of the modulator (wiggler) as a function of its gap. K is computed from magnetic measurements performed before the wiggler installation.

coordinates and velocities in the horizontal and vertical planes, while t is the longitudinal coordinate and $\delta E/E$ is the energy shift from the particle reference energy.

The modulator (wiggler) is defined by its magnetic period λ_w , its number of periods N_w (see Table 1) and its deflection parameter K . The K values, as presented in Fig. 5, depend on the wiggler gap and were computed using the magnetic measurements of the wiggler field before its installation. Both *GENESIS* and *ELEGANT* assume an ideal (purely sinusoidal) magnetic field.

The laser pulse longitudinal intensity is defined in the *GENESIS* code as the following,

$$I(t) = P(t) \cos[\omega_L t - \varphi(t)]. \quad (1)$$

$P(t)$ is the longitudinal power, the maximum of which corresponds to the pulse peak power, while $\varphi(t)$ is the phase, with $\omega_L = 2\pi c/\lambda_L$ the central angular frequency of the electric field of the laser pulse. Both $P(t)$ and $\varphi(t)$ are deduced from the Fourier transform of the complex electric field in the frequency domain $\tilde{E}(\omega) = [(4\pi/\epsilon_0 c) \tilde{I}(\omega)]^{1/2} \cos[\Phi(\omega)]$, where $\tilde{I}(\omega)$ is the spectral intensity and $\Phi(\omega)$ is the spectral phase of the pulse. The spectrum $\tilde{I}(\omega)$ was measured by means of a fiber spectrometer. The spectral phase $\Phi(\omega)$ was approximated by the second-order term of its Taylor expansion near ω_L , following $\Phi(\omega) \simeq A(\omega - \omega_L)^2$. In this approximation, the laser chirp can be modified *via* the A parameter to change the pulse duration. In the case of *ELEGANT*, the laser power temporal profile was assumed to be Gaussian, the inputs being the peak power and the FWHM of the power temporal profile. In both cases, the laser focusing is described by a Rayleigh length Z_R and a focusing location inside the wiggler. According to the experimental results presented in Fig. 2, we took for the simulations the standard focusing setting around $f\# \simeq 2$ and assumed that it corresponded to a waist of $300 \mu\text{m}$ at 800nm for a perfect diffraction-limited laser beam, *i.e.* a Z_R of 0.35m , located at the center of the wiggler.

Finally, *GENESIS* as well as *ELEGANT* compute the evolution of the electron beam six-dimensional phase space inside the magnetic field of the wiggler, integrating Maxwell equations at each wiggler period. Fig. 6(a) presents a typical

energy distribution as a function of the longitudinal coordinate t , obtained at the wiggler exit using *GENESIS*. With a 0.4mJ energy pulse, the energy is modulated with a maximum amplitude of $\Delta E = 20 \text{MeV}$. *ELEGANT* and *GENESIS* results in the sliced region are compared in Fig. 6(b) in terms of number of particles per energy, and found to be in good agreement.

3.2. THz emission at the AILES beamline

For the THz emission modelling, the interaction is simulated with *GENESIS*. In this case, since the chromatic sorting of the particles (inherent to the storage in the ring of a non-zero energy spread beam) showed negligible effects on the final THz signal, it was not included in the modelling, which also enabled to speed up the calculations. The six-dimensional electron beam distribution provided by *GENESIS* at the wiggler exit is projected over the x and y axis to provide the electron beam temporal energy distribution. This two-dimensional $(t, \delta E/E)$ distribution is then transported along the storage ring assuming a linear transformation of those coordinates using the transport matrix formalism (Byrd *et al.*, 2006),

$$t \rightarrow t + R_{56} \delta E/E. \quad (2)$$

The transverse dynamics is neglected since simulations revealed no significant impact on the longitudinal distribution. This simple model enables the electron beam distribution to

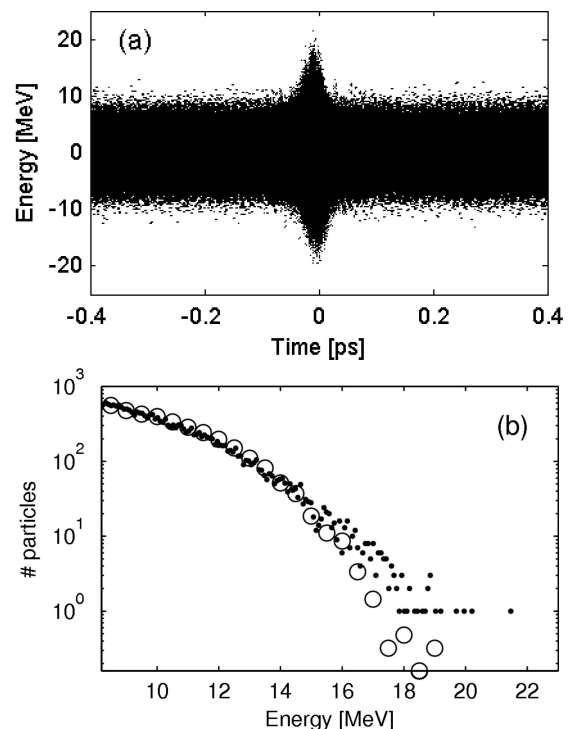


Figure 6
Energy distribution (with respect to the reference energy) of the electron beam at the wiggler exit. (a) Longitudinal energy distribution computed with *GENESIS*. (b) Number of particles *versus* energy computed with (dots) *GENESIS* and (circles) *ELEGANT*. $E_{\text{Laser}} = 0.4 \text{mJ}$, $Z_R = 0.35 \text{m}$, $\Delta T = 35 \text{fs}$ FWHM, gap = 17mm .

be computed at any source point along the ring, not only at its very first pass after the interaction but also after several revolutions as illustrated in Fig. 7(a).

Because R_{56} is a non-zero term, the particles rotate in the phase space, converting the energy modulation into a density modulation. Projecting the temporal energy distribution to obtain the beam longitudinal profile reveals a hole in the region where the laser interacted with the electron beam (Holldack *et al.*, 2006). This longitudinal profile is then fitted with a sum of four Gaussian functions: one for the core beam with a typical duration of 30 ps RMS, one for the main ‘hole’ with a typical duration of 1 ps and two for the wings that appear on the hole edges. Typical profiles obtained at the AILES beamline are presented in Fig. 7(b). The hole width at the AILES beamline is typically 1 ps FWHM at the first turn, and progressively vanishes turn after turn.

When the electron beam duration or some structures in the electron beam come close to the radiation wavelength, the emitted synchrotron radiation becomes coherent and its

frequency distribution can be expressed according to (Wiedemann, 1993)

$$\frac{dP_{\text{coh}}}{d\nu} = N_e \text{FF}(\nu) \frac{dP_{\text{inc}}(\nu)}{d\nu}. \quad (3)$$

N_e is the number of electrons, $P_{\text{inc}}(\nu)$ is the incoherent synchrotron radiation, while $\text{FF}(\nu)$ is the so-called form factor, given by the square of the Fourier transform in the frequency domain of the electron beam longitudinal distribution $\rho(t)$. In the SOLEIL setup case, since the hole structure is typically 1 ps, coherent radiation is expected in the THz range.

The form factor is here computed using the four Gaussian fits result for each of the first three turns. After more than three turns, the longitudinal profiles are too noisy to provide significant results. Typical form factors are presented in Fig. 7(c). In good agreement with expectations (frequency in the Fourier space of a picosecond period signal), the form factor at the first turn is found to be maximum at around 0.4 THz. In addition, it clearly appears that while the hole vanishes, *i.e.* presents a wider width, the form factor spectral content shifts to lower frequencies. At the third turn, the frequency at the form factor peak value is already below 0.1 THz. It is also important to note that, even if the frequency at the form factor peak value decreases, this peak value is rather constant at least from the first to the second turn.

Using the calculation methodology mentioned above, Fig. 8 presents a systematic study of the form factor looking at its peak value and frequency at peak value, as a function of the wiggler gap and laser pulse energy over the first two turns in the machine.

3.2.1. Dependence of the form factor on the wiggler gap value. Both first- and second-turn form factors (see Fig. 8c)

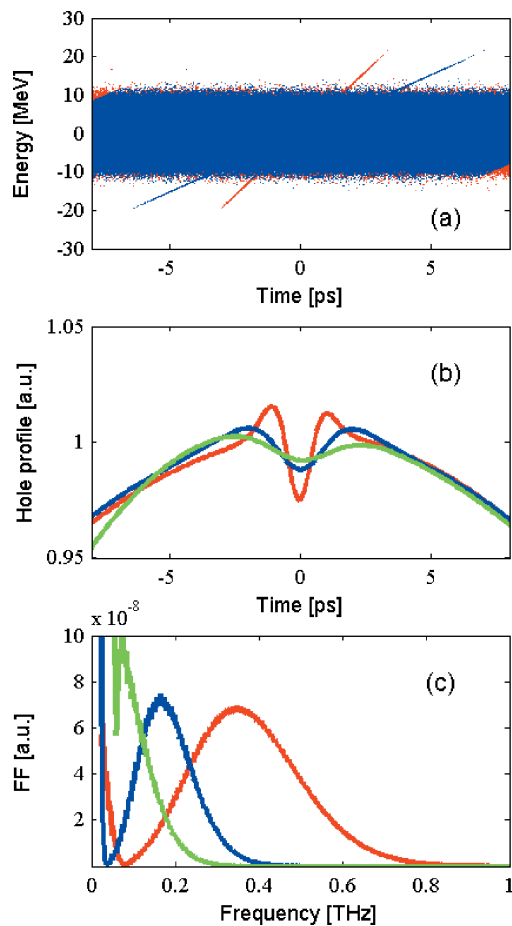


Figure 7 Electron beam modelling at the AILES beamline at the first (red), second (blue) and third (green) turn after interaction. (a) Longitudinal energy distribution with respect to the reference energy. (b) Longitudinal density profile corresponding to the projection of (a). (c) Form factor. Interaction simulated with *GENESIS* using $E_{\text{Laser}} = 0.4$ mJ, $Z_R = 0.35$ m, $\Delta T = 35$ fs FWHM, gap = 17 mm. Energy distribution not displayed for the third turn for the sake of clarity.

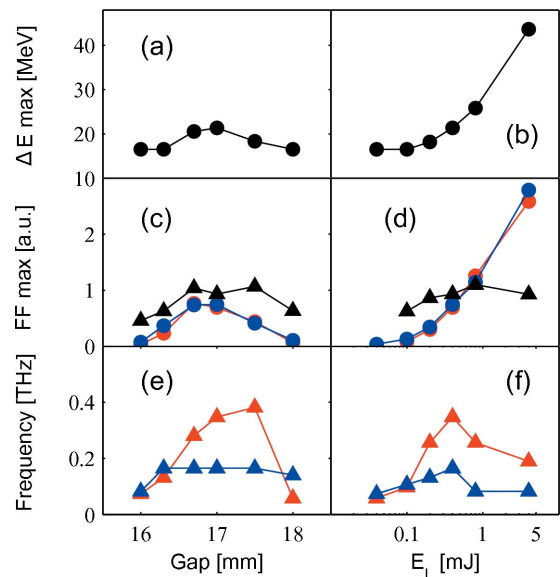


Figure 8 (a, b) Maximum energy exchange, (c, d) form factor peak value and (e, f) form factor frequency at its peak value, calculated as a function of (a, c, e) wiggler gap for $E_{\text{Laser}} = 0.4$ mJ and (b, d, f) laser pulse energy for a gap of 17 mm. In (c)–(f), (red dots) first turn and (blue dots) second turn. In (c), (black triangles) ratio of first over second-turn form factor maximum intensities. $\Delta T_{\text{Laser}} = 35$ fs FWHM, $Z_R = 0.35$ m.

reach their maximum peak value for a wiggler gap around 16.8 mm, *i.e.* around the resonance condition $\lambda_R = \lambda_L$. Simultaneously (see Fig. 8a), the maximum energy exchange is reached (around 20 MeV in the case presented here). The form factor peak value at the first turn is similar to the one at the second turn around the resonance, and slightly lower far from resonance.

The first-turn form factor frequency at its peak value varies between 0.1 and 0.4 THz as the gap increases between 16 and 18 mm (see Fig. 8e). On the contrary, the second-turn form factor frequency at its peak value hardly depends in the wiggler gap. One notes that maximizing the peak value of the form factor at the first turn tends to increase this central frequency.

3.2.2. Dependence of the form factor on the laser pulse energy. Over two decades of laser pulse energy, the peak value of both the first- and second-turn form factors (see Fig. 8d) keep increasing, just as the maximum energy exchanged. The form factor peak values scale roughly as the square of the laser pulse energy, as expected from theory (Evain *et al.*, 2010), while the first turn peak value remains similar to the second-turn one. Looking at the evolution of the form factor frequencies at their peak value (see Fig. 8f), again we observe little dependence in the case of the second turn. As for the first turn, the form factor frequency at its peak value first increases up to 0.4 THz and then decreases back to 0.2 THz. This behaviour is essentially due to the shape of the hole which exhibits side ‘bumps’ increasingly distorting the simple initial Gaussian profile as the laser pulse energy increases (see Fig. 7b).

Finally, the incoherent synchrotron radiation spectral intensity presented in Fig. 4 is convoluted to the form factor to derive the coherent THz power produced by the interaction according to equation (3). Then, to fully predict the diagnostics signals, $dP_{\text{coh}}/d\nu$ is convoluted to the diagnostic responses given in Fig. 4.

Fig. 9(i-a) clearly shows that the spectrometer essentially detects the first turn: the contribution of the second turn is found to be negligible (two orders of magnitude lower in intensity) while that of the third turn is completely suppressed by the optics inside the spectrometer. Looking at the evolution of the spectrometer signal as a function of the wiggler gap and laser power, Figs. 9(ii-a)–9(ii-d), reveals that, as the form factor, the spectrometer maximum intensity can be optimized as a function of the wiggler gap (with an optimum around 17 mm) and can be maximized increasing the laser pulse energy. But the behaviour of the spectrometer signal frequency at maximum intensity significantly differs from that of the

form factor, both *versus* wiggler gap and laser pulse energy. Because the spectrometer spectral response dramatically favours high frequencies, the spectrometer signal frequency at maximum intensity is indeed not maximum but minimum near the resonance and increasing the laser pulse energy tends to decrease this frequency towards a lower limit around 0.5 THz.

Thanks to its higher efficiency at low frequencies, the bolometer is expected to detect at least both the first and the second-turn signals [see Fig. 9(i-b)]. The signal amplitude *versus* wiggler gap and laser pulse energy keeps following the same evolution as the form factor and the maximum energy exchange, with an optimum around 17 mm and no maximum reached *versus* laser energy. In addition, the amplitude of the first-turn signal seems to increase faster than that of the second turn when increasing the wiggler gap to slightly above the resonance, or increasing the laser energy. This relative amplitude evolution is enhanced with respect to the initial case of the form factor because of the bolometer spectral response. It is also the case for the bolometer signal frequency at maximum intensity [see Figs. 9(i-b) and 9(i-d)] which, as the spectrometer, tends to exhibit a minimum *versus* wiggler gap and to decrease *versus* laser pulse energy.

3.3. Electron beam simulation at source points

The particle distribution at the expected source points is obtained in two successive steps. The interaction in the wiggler is first simulated with *ELEGANT* taking into account the initial chromatic sorting of the particles in the non-zero dispersion straight section of the wiggler. Then a six-dimensional tracking around the ring is performed with *Accelerator*

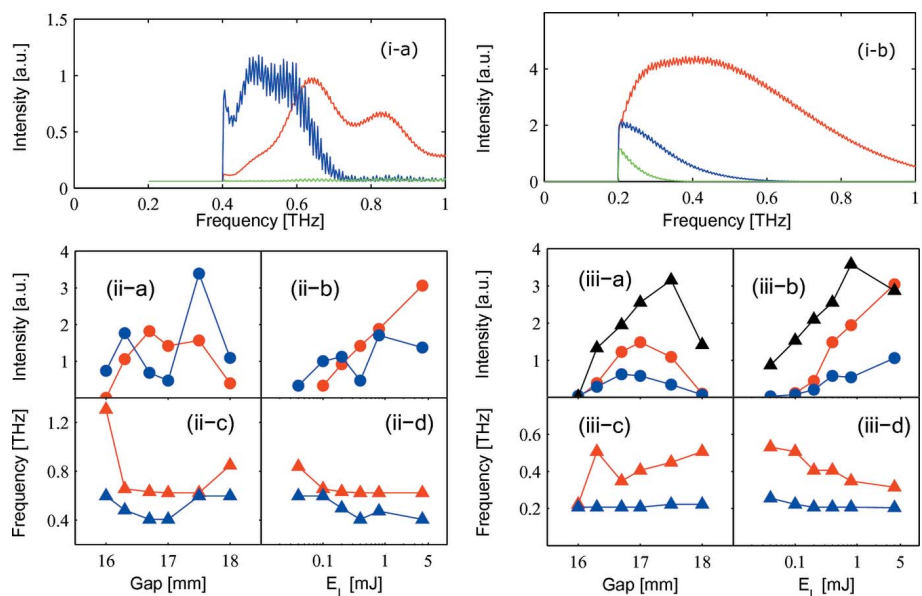


Figure 9 (i) Spectral intensity of the (a) spectrometer (with turn 2×100) and (b) bolometer, calculated for $E_L = 0.4$ mJ and gap = 17 mm. (ii) Spectrometer and (iii) bolometer maximum intensity and frequency of maximum intensity *versus* wiggler gap calculated for $E_L = 0.4$ mJ and *versus* E_L for gap = 17 mm. In all plots, red lines or dots represent the first, blue the second and green for the third turn. In (ii-a) and (ii-b), second-turn intensity $\times 100$. In (iii-a) and (iii-b), black triangles represent the ratio first over second-turn form factor maximum intensities. $Z_R = 0.35$ m and $\Delta T = 35$ fs FWHM.

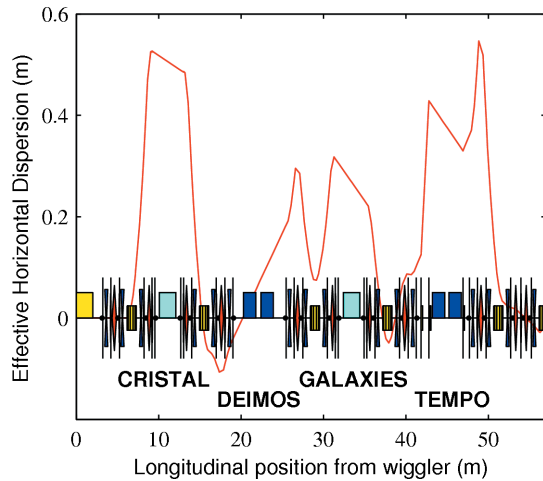


Figure 10 Effective horizontal dispersion function at SOLEIL experienced by the off-energy ‘sliced’ electrons, from the interaction point with the laser to downstream source points (CRISTAL, DEIMOS, GALAXIES and TEMPO beamlines). Simulation with the *AT* code.

Toolbox (AT) (Terebilo, 2001). The non-linear effects of the optics are included, as required when considering the large transverse and longitudinal oscillations of the slices. The SOLEIL optics is the one established for normal user operation (Brunelle *et al.*, 2011, with only slight modifications).

A special feature of the femtoslicing scheme at SOLEIL consists of using the natural horizontal dispersion function of the machine to separate the sliced electrons from the core electron beam. The effective dispersion experienced by the energy-modulated electrons downstream of the wiggler is shown in Fig. 10. The effect of this dispersion on the beam horizontal phase space at the first source point, *i.e.* inside the CRISTAL undulator, is shown in Fig. 11. The particles are clearly spread out allowing removal of (i) the contribution from the core by means of a diaphragm placed at the front-end and shifted by a few millimeters (red lines in Fig. 11) and (ii) the contribution from the halo by means of a movable slit at the very end of the beamline, close to the sample position (black lines in Fig. 11). The halo consists of particles which exchanged energy in previous interaction cycles, and that remain inside the machine acceptance while damping slowly to equilibrium with a typical damping time of 7 ms, *i.e.* much slower than the laser repetition rate. Moreover, decoherence causes a fast filamentation of this halo (Meller *et al.*, 1987), filling up the horizontal phase space. The halo potentially radiates in the beamline acceptance, leading to an undesirable background because of its duration lying in the picosecond range. It is thus important to achieve an efficient screening of the halo beam contribu-

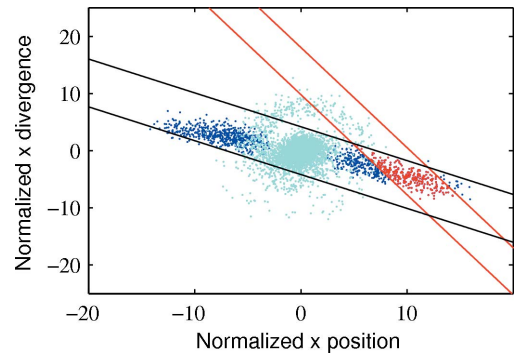


Figure 11 Simulated horizontal phase space of the sliced electrons in the U20 undulator of the CRISTAL beamline. Phase space normalized to σ_x and σ'_x of the beam at equilibrium state. Particles in dark blue represent the last interaction, *i.e.* first pass in the undulator, red represents emitting photons within the beamline acceptance, and light blue previous interactions, *i.e.* halo. Red lines: front-end diaphragm acceptance. Black lines: slit acceptance at the very end of the beamline. Simulation with *ELEGANT* and *AT* using $E_{\text{Laser}} = 1.5$ mJ, $\Delta E_{\text{Max}} = 30$ MeV, $\Delta T_{\text{Laser}} = 35$ fs FWHM, $Z_R = 0.35$ m, $M^2 = 1.0$, gap = 16.7 mm.

tions, keeping contamination rates below a few percent (Ciavardini *et al.*, 2017; Streun, 2010).

Fig. 12(a) then presents horizontal phase spaces at source points further downstream, *i.e.* the DEIMOS, GALAXIES and TEMPO beamlines. While slice separation on CRISTAL essentially resulted from the horizontal dispersion amplitude, an additional contribution from the horizontal dispersion angle comes for the following source points. The projection in the longitudinal plane of the phase spaces provides the temporal distribution of both positive (positive energy gain) and negative slices. All beamlines chose to use the positive slice in order to minimize the contribution to the background emission from the closest upstream dipole, and, as depicted in Fig. 12(b), the natural stretching of the positive slice along the non-isochronous ring remains acceptable from the wiggler straight section (75 fs FWHM) down to the CRISTAL (140 fs

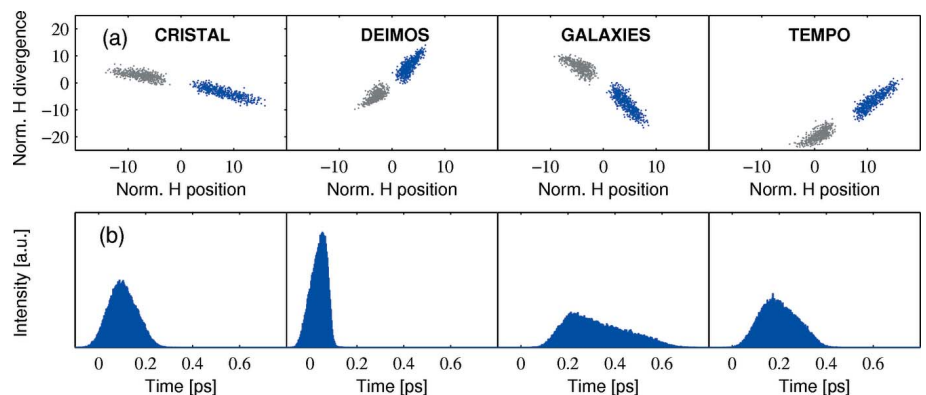


Figure 12 Simulated electron beam distributions at the source point of four beamlines, for sliced electrons with absolute energy gain above $3\sigma_E$ in (a) the horizontal phase space for positive (blue) and negative (grey) slices, normalized to σ_x and σ'_x of the beam at equilibrium state, and in (b) the temporal dimension for the positive slice. For TEMPO, the whole beam was displaced by a magnetic chicane to drive the positive slice on the beamline axis. Simulation with *ELEGANT* and *AT*, using $E_{\text{Laser}} = 1.5$ mJ, $\Delta T_{\text{Laser}} = 35$ fs FWHM, $Z_R = 0.35$ m, $M^2 = 1.0$, gap = 16.7 mm.

FWHM), DEIMOS (80 fs FWHM), GALAXIES (300 fs FWHM) and TEMPO (210 fs FWHM) beamlines, located 50 m downstream of the modulator wiggler. These numbers are given in the case of a maximum laser–electron energy exchange of 30 MeV (using a laser energy of 1.5 mJ) but a lower level of energy exchange would lead to even shorter slice durations at the source points. Note that the dispersive coefficient R_{56} of the linear transfer matrix decreases locally at the DEIMOS beamline (<http://www.synchrotron-soleil.fr/Recherche/LignesLumiere/DEIMOS>), leading to a shorter slice.

In order to optimize the photon collection of the CRISTAL and TEMPO beamlines during their commissioning phase, a simple model of photon emission is then used at the beamline source points. Each electron from the previously described simulation is associated with one photon, the spectrum of which corresponds to the spectrum of a zero energy spread but non-zero emittance electron beam. In the case of the hard X-ray beamline CRISTAL, we also considered a zero photon emittance. This model will also be used in the near future to study the halo contribution to the background signal in the framework of femtoslicing experiments at higher repetition rate (5 kHz).

4. Experimental determination of the energy exchange using the THz signals

The commissioning phase enabled extended measurements of THz signals which, after comparison with the model, first allowed a successful interaction in the wiggler to be shown and then the level of this interaction to be estimated.

4.1. Typical interaction evidence

Fig. 13(a) reports the maximum intensity of the bolometer signal as a function of the peak current of the sliced bunch. Peak current values were derived from the measured average current I (using a DC current transformer) and the measured bunch length *versus* I (using a streak camera). As expected for a coherent signal, the THz intensity scales as the square of the peak current. The maximum intensity of the bolometer signal was also recorded as a function of the wiggler gap, *i.e.* for various resonance wavelengths λ_R [see Fig. 13(b)]. The optimum is reached for a gap between 16.9 and 17 mm corresponding to a resonance wavelength of 767 nm, in good agreement with the model results [see Fig. 9(iii-a)].

To avoid the saturation of the bolometer at the nominal 5 mA current for operation, the coherent synchrotron radiation has to be attenuated with filters. Fig. 14 shows that the effect of the filters is significantly different on each turn. Using a fused silica filter [see Fig. 14(a)] tends to attenuate more strongly the first (by a factor of 26) than the second (factor of 10) turn, whatever the gap. The transmission of the fused silica filter is known to decrease linearly from 0.1 THz to 2 THz which clearly indicates that the frequency content of the first turn is different and in a higher-frequency region than the content of the second turn. In addition, taking into account the

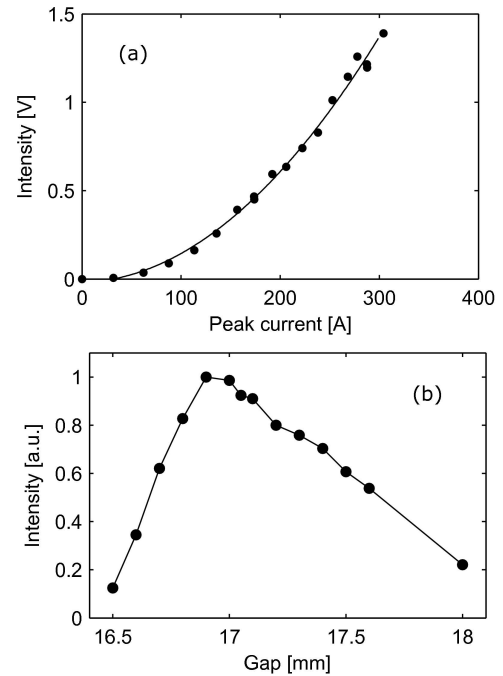


Figure 13 (a) Maximum intensity of the bolometer signal averaged over ten shots *versus* electron beam peak current. Black circles: experiment. Black line: quadratic fit. $P_{\text{Laser}} = 0.6$ W, $\Delta T_{\text{Laser}} = 500$ fs FWHM ± 100 fs, $f\# = 4.5$, wiggler gap = 17.1 mm. (b) Normalized maximum intensity of the bolometer signal *versus* wiggler gap. $P_{\text{Laser}} = 5.1$ W, $\Delta T_{\text{Laser}} = 35$ fs FWHM, $f\# = 2$, $I = 5$ mA in the single bunch of the hybrid mode of operation.

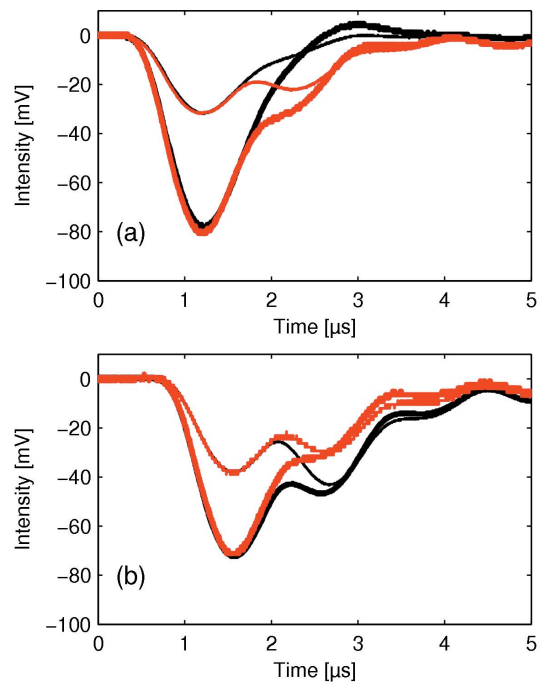


Figure 14 (a) Bolometer traces with (red) and without (black) the fused silica filter, together with the metallic grid filters. (b) Bolometer traces with (red) and without (black) the metallic grid filters, together with the fused silica filter. In both (a) and (b), the traces with filter are scaled to match at maximum the traces without filter. Thick lines for 17 mm gap and thin lines for 16.7 mm gap. (a) $P_{\text{Laser}} = 2.6$ W and $f\# = 1.3$, (b) $P_{\text{Laser}} = 2$ W and $f\# = 0.3$, and for both (a) and (b) $\Delta T_{\text{Laser}} = 35$ fs FWHM.

transmission rate of the filter (10% at 0.4 THz), both turn contents should range below 0.6 THz. Both observations are found to be in good agreement with the model predictions. Using metallic grid filters [see Fig. 14(b)], acting as high-pass filters, we observed a stronger attenuation of the second turn. In agreement with the previous observations and the model, the second turn seems to produce lower THz frequency radiation than the first turn.

4.2. THz optimization and turn-by-turn ratio

According to the model (see Figs. 8 and 9), the efficiency of the energy exchange is expected to scale as the THz intensity measured at the AILES beamline. The THz signal was therefore optimized, essentially as a function of the wiggler gap and laser power. The optimum gap ranged between 16.8 and 17.1 mm, slightly depending on the laser power. There is no optimum in terms of power: the THz intensity keeps increasing up to the maximum available laser energy (5 mJ in the laser hutch, *i.e.* about 3.4 mJ inside the wiggler) in the available focusing range.

Using a fixed set of filters, the relative amplitudes of the first and second turns recorded with the bolometer have been analyzed. As illustrated in Fig. 15, near the optimum gap the second turn becomes barely visible, while the first and the second turn can become of equivalent intensity far from the resonance. The amplitude of the first turn increases much faster than the amplitude of the second turn up to the optimum gap, above which both amplitudes decrease at the

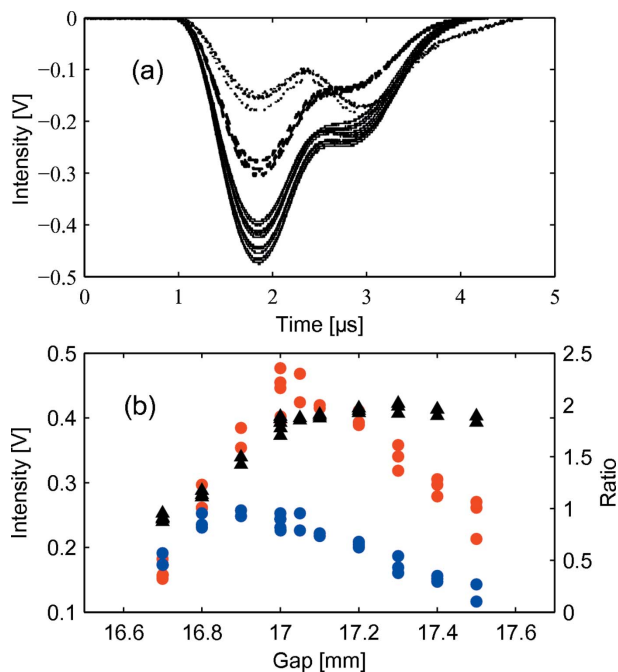


Figure 15 Bolometer signal *versus* gap. (a) Bolometer signal for gaps (dotted lines) below 16.7 mm, (full line) between 16.9 and 17.1 mm, (dashed line) above 17.4 mm. (b) Absolute maximum intensity of the (red) first and (blue) second turn and (black) ratio first over second-turn maximum intensity. $P_{\text{Laser}} = 3.8$ W, $f\# = 1.0$, $\Delta T_{\text{Laser}} = 35$ fs FWHM, $I = 5$ mA in single-bunch mode, with fused silica filter.

same rate. This behaviour is found in very good agreement with the predictions of Fig. 9(iii-a).

We also observed that increasing the laser power clearly enhanced the first turn with respect to the second turn, which is again found in good agreement with the predictions of Fig. 9(iii-b).

Those preliminary observations confirmed a successful interaction of the laser with the electron beam inside the wiggler.

4.3. THz spectra measurements and interaction level

For further insight into this interaction, the spectrum of the THz field was measured in dedicated beam times using the AILES spectrometer. Because the laser is injected at 1 kHz while the electron beam revolution frequency is 846 kHz, the laser-ON spectra recorded correspond in fact to the sum of laser-ON spectra at 1 kHz and laser-OFF spectra at 846 kHz (incoherent synchrotron radiation spectra) integrated over several seconds.

Fig. 16 presents laser-ON spectra, which exhibit a bell-shape with a frequency at maximum intensity around 0.6 THz in agreement with the predictions of Fig. 9(i-a). Varying the gap essentially modifies the amplitude of the spectra. In the case of a low-energy laser (Fig. 16a), the frequency at maximum intensity is constant *versus* gap and found close to 0.7 THz. In the case of a high-energy laser (Fig. 16b), the frequency at maximum intensity varies with the gap: the minimum

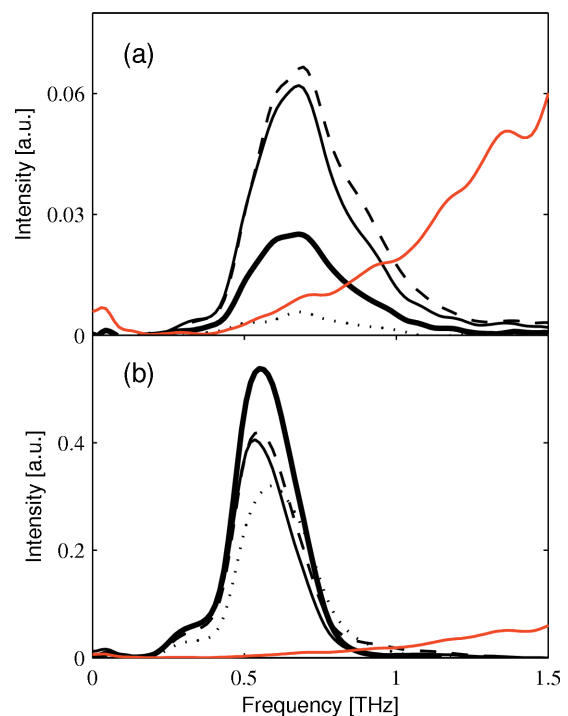


Figure 16 THz field spectra recorded on the AILES beamline with (black) laser-ON and (red) laser-OFF ($\times 100$) for (a) $P_{\text{Laser}} = 0.3$ W and (b) $P_{\text{Laser}} = 2.6$ W. For laser-ON lines, the gap is (dotted line) 16.7 mm, (thick full line) 16.9 mm, (thin full line) 17.2 mm and (dashed line) 17.5 mm. $\Delta T_{\text{Laser}} = 35$ fs FWHM, $f\# = 1.3$, $I = 5$ mA in single-bunch mode.

frequency is reached simultaneously with the maximum amplitude close to 0.5 THz. Far from the resonance, this frequency increases back to 0.7 THz. All those behaviours match the predictions of Figs. 9(ii-a)–9(ii-d). Still, note that a shift of the optimum wiggler gap is observed between low and high laser energy: decreasing the laser energy shifts the resonance to higher gaps, *i.e.* smaller wavelengths. This is probably due to a chromatic effect in the focusing lenses of the laser transport which is not reproduced by the model.

Figs. 17 and 18 finally enable our spectra measurements to be compared in more detail with the model. In Fig. 17 (Fig. 18), the spectra maximum intensities (frequencies at maximum intensity) for two different focusing settings $f\#$ are plotted as a function of the laser power. In both experimental and modelled cases, the displayed laser power is the ‘initial’ power, *i.e.* the laser power measured in the laser hutch prior to transport and associated losses in the experimental case and the laser power prior to applying an efficiency coefficient before simulating the energy exchange in the modelling case. The measured spectra were recorded for two different gap settings (blue and red dots in the figures). As expected, the maximum THz intensity first increases as the square of the laser power before starting to saturate. In parallel, the frequency at maximum intensity also shifts towards lower frequencies (~ 0.5 THz). The measurements are directly compared with the model (black lines in the figures) assuming

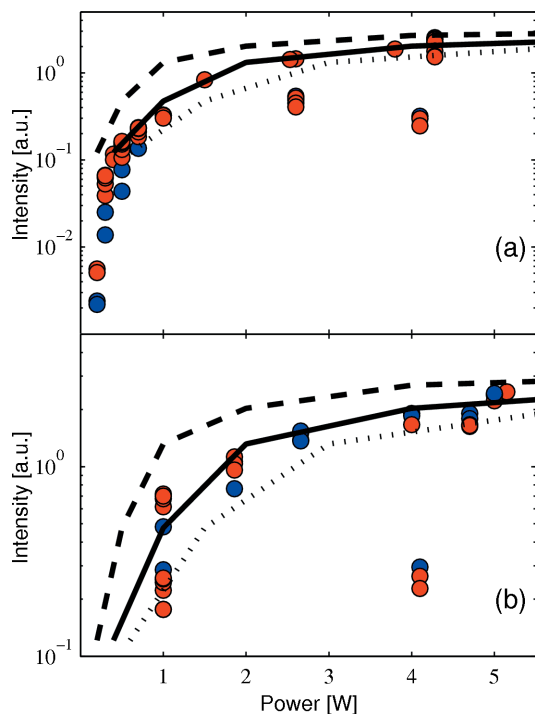


Figure 17 Maximum intensity of the spectra recorded on the AILES beamline versus laser power for two focusing settings: (a) $f\# = 1.3$ and (b) $f\# = 2.5$. Spots for experimental data with (blue spots) $16.8 \leq \text{gap} < 17$ mm and (red dots) $17 \leq \text{gap} < 17.5$ mm. Lines for simulations using $\Delta T_{\text{Laser}} = 35$ fs FWHM, $Z_R = 0.35$ m at gap = 17 mm and an efficiency coefficient of (dotted line) 5, (full line) 10 and (dashed line) 15% on the laser power (*i.e.* for instance while 2 W are sent from the laser hutch, $2 \text{ W} \times 15\% = 0.3 \text{ W}$ are actually used for the simulation).

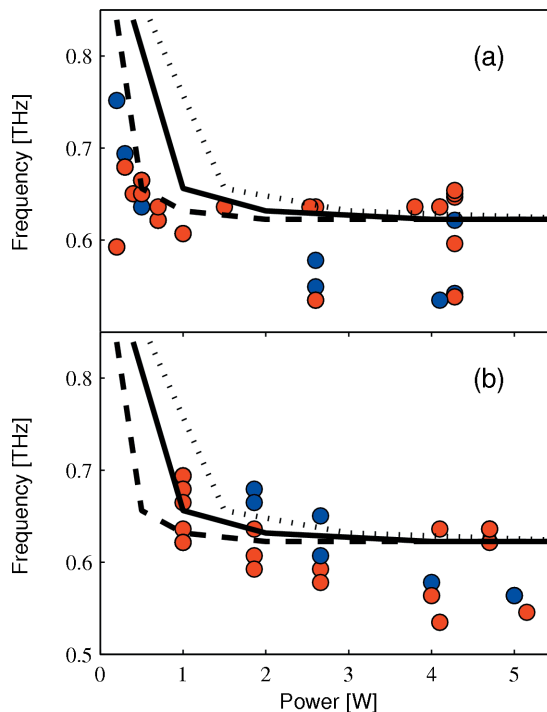


Figure 18 Frequency at maximum intensity of the spectra recorded on the AILES beamline versus laser power for two focusing settings: (a) $f\# = 1.3$ and (b) $f\# = 2.5$. Spots for experimental data with (blue spots) $16.8 \leq \text{gap} < 17$ mm and (red dots) $17 \leq \text{gap} < 17.5$ mm. Lines for simulations using $\Delta T_{\text{Laser}} = 35$ fs FWHM, $Z_R = 0.35$ m at gap = 17 mm and an efficiency coefficient of (dotted line) 5, (full line) 10 and (dashed line) 15% on the laser power.

different values for the efficiency coefficient. The best fit is obtained for an efficiency of 10% applied to the laser pulse energy measured in the laser hutch. This would indicate that, when the 5 W available are sent experimentally towards the wiggler, only 0.5 W are effectively ‘used’ for the energy exchange, leading to a maximum energy modulation of about 18 MeV as shown in Fig. 6(a). As detailed previously, the transmission of the laser power through the transport line down to the wiggler was measured to be less than 68% in standard operation. The model therefore indicates an interaction efficiency more than six times lower than expected. Such discrepancy might essentially be due to a laser wavefront distortion occurring in the vacuum pipes during the transport. Those pipes are known indeed to be too narrow to allow a free path of the laser beam. Additional losses could also be due to a non-perfect overlap between the electron beam and the laser along the wiggler, resulting from laser pointing instabilities or from a non-perfect trajectory of the electron beam in the wiggler magnetic field.

5. First multi-beamline femtoslicing operation

Fig. 19 presents the simultaneous record, in femtoslicing operation, of the coherent THz intensity together with the slice photon flux on both CRISTAL and TEMPO beamlines. It is the first demonstration of a multi-beamline femtoslicing facility. The optimum gap is the same for both beamlines, and

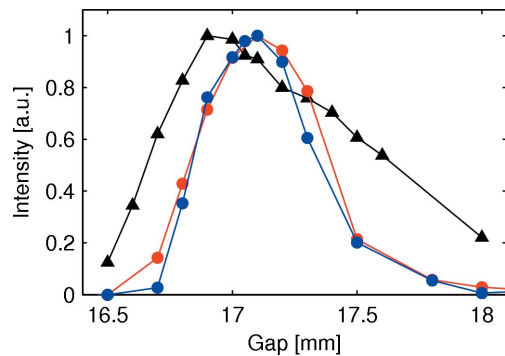


Figure 19

Simultaneous record of the (black triangles) THz intensity and slice photon flux on the (red dots) CRISTAL and (blue dots) TEMPO beamlines. $P_{\text{Laser}} = 5.1$ W, $\Delta T_{\text{Laser}} = 35$ fs FWHM, $f_{\#} = 2$, $I = 5$ mA in the single bunch of the hybrid mode of operation.

slightly different than the one for the THz intensity. This can be understood as the maximum photon flux is reached on both beamlines when the positive slice charge is maximized, while the maximum THz intensity is reached when the hole depth is maximized. The CRISTAL and TEMPO beamlines can now use the sub-picosecond pulses for time-resolved studies in the hard and soft X-ray range, respectively. With a slicing efficiency as described in §4.3, the number of photons foreseen at the CRISTAL beamline ranges around 80 photons pulse⁻¹ for a bandwidth of 2×10^{-4} , according to ray-tracing simulations.

6. Conclusion and perspectives

This paper summarizes the commissioning of the femtoslicing source at SOLEIL. In the experimental scheme adopted, the electron beam energy is set as high as 2.75 GeV and the slice separation relies solely on the natural dispersion function, while other femtoslicing setups have been using lower beam energies and relied on chicanes for the slice separation.

We give evidence for a significant interaction between the laser and the electron beam, by reporting the detection of a clear coherent THz signal on the AILES beamline. A refined tool was developed to model this coherent THz signal and the expected response of the various THz detectors used. The main features of the diagnostic traces used (bolometer and spectrometer) were found to be in very good agreement with the predictions. In addition, the analysis of the recorded spectra dependence on the laser power showed that approximately 10% of the available laser power in the hutch was effectively used for the energy exchange, while an efficiency of about 68% was expected from our measurements. The maximum energy modulation achieved would then be around 18 MeV. The discrepancy between the retrieved and measured efficiencies may essentially be due to a strong laser beam wavefront distortion in the transport line. This efficiency issue has been addressed and will be worked out during the laser shutdown for upgrade (until mid-2018).

As a very important point, we also showed that not only one but two beamlines can use the sub-picosecond duration bunch simultaneously. The CRISTAL beamline has even already

successfully implemented pump-probe experiments (Ciavardini *et al.*, 2018) while TEMPO is expecting users by the end of 2018.

Although preventing femtoslicing experiments for a few months, the on-going laser upgrade to 5 kHz will allow a new range of beam dynamics regimes to be studied, which may become critical, and therefore challenging, in terms of halo for instance.

Acknowledgements

The authors would like to thank the Accelerator and Engineering Division of SOLEIL for their essential support all along the commissioning phase, as well as the whole AILES beamline for their help in the implement, operation and analysis of the THz diagnostics. The authors are also grateful to S. Bielawski's group from PhLAM, and in particular to E. Roussel, for fruitful discussions on the THz emission modelling.

Funding information

Funding for this research was provided by: Agence Nationale de la Recherche (DYNACO contract No. ANR-10-BLAN-0423).

References

- Ackermann, W. *et al.* (2007). *Nat. Photon.* **6**, 336–342.
- Allaria, E. *et al.* (2012). *Nat. Photon.* **10**, 699–704.
- Beaud, P., Johnson, S. L., Streun, A., Abela, R., Abramsohn, D., Grolimund, D., Krasniqi, F., Schmidt, T., Schlott, V. & Ingold, G. (2007). *Phys. Rev. Lett.* **99**, 174801.
- Bielawski, S., Evain, C., Hara, T., Hosaka, M., Katoh, M., Kimura, S., Mochihashi, A., Shimada, M., Szwaj, C., Takahashi, T. & Takashima, Y. (2008). *Nat. Phys.* **4**, 390–393.
- Borland, M. (2000). *Proceedings of the 2000 International Conference on Atomic Physics*, Florence, Italy, 4–9 June 2000. LS-287.
- Brubach, J. B., Manceron, L., Rouzières, M., Pirali, O., Balcon, D., Tchana, F. K., Boudon, V., Tudorie, M., Huet, T., Cuisset, A., Roy, P., Predoi-Cross, A. & Billinghamurst, B. E. (2010). *AIP Conf. Proc.* **1214**, 81–84.
- Brunelle, P., Couprie, M.-E., Denard, J.-C., Filhol, J.-M., Lamarre, J.-F., Lebasque, P., Loulergue, A., Marchand, P., Nadji, A., Nadolski, L. S., Nagaoka, R. & Tordeux, M.-A. (2011). *Proceedings of the 2011 International Particle Accelerator Conference*, San Sebastian, Spain, 4–9 September 2011, pp. 2124–2126.
- Byrd, J. M., Hao, Z., Martin, M. C., Robin, D. S., Sannibale, F., Schoenlein, R. W., Zholents, A. A. & Zolotarev, M. S. (2006). *Phys. Rev. Lett.* **96**, 164801.
- Ciavardini, A. *et al.* (2018). In preparation.
- Dalla Bernardina, S., Alabarse, F., Kalinko, A., Roy, P., Chapuis, M., Vita, N., Hienerwadel, R., Berthomieu, C., Judeinstein, P., Zanotti, J.-M., Bantignies, J. L., Haines, J., Catafesta, J., Creff, G., Manceron, L. & Brubach, J.-B. (2014). *Vibr. Spectrosc.* **75**, 154–161.
- Emma, P. *et al.* (2010). *Nat. Photon.* **9**, 641–647.
- Evain, C. *et al.* (2010). *Phys. Rev. ST Accel. Beams*, **13**, 090703.
- Evain, C., Loulergue, A., Nadji, A., Filhol, J. M., Couprie, M. E. & Zholents, A. A. (2012). *New J. Phys.* **14**, 023003.
- Hollmack, K. *et al.* (2005). *Phys. Rev. ST Accel. Beams*, **8**, 040704.
- Hollmack, K., Khan, S., Mitzner, R. & Quast, T. (2006). *Phys. Rev. Lett.* **96**, 054801.

- Hosaka, M., Yamamoto, N., Takashima, Y., Szwaj, C., Le Parquier, M., Evain, C., Bielawski, S., Adachi, M., Zen, H., Tanikawa, T., Kimura, S., Katoh, M., Shimada, M. & Takahashi, T. (2013). *Phys. Rev. ST Accel. Beams*, **16**, 020701.
- Ishikawa, T. *et al.* (2012). *Nat. Photon.* **8**, 540–544.
- Labat, M. *et al.* (2014). *Proceedings of the 2014 International Particle Accelerator Conference*, Dresden, Germany, pp. 206–208.
- Laulhé, C., Cammarata, M., Servol, M., Miller, R. J. D., Hada, M. & Ravy, S. (2013). *Eur. Phys. J. Spec. Top.* **222**, 1277–1285.
- Laulhé, C., Ravy, S., Fertey, P., Elkaim, E., Legrand, F., Féret, P., Hollander, P., Hustache, S., Bordessoule, M., Ricaud, J. P., Collet, E., Lorenc, M., Buron-Le Cointe, M., Cailleau, H., Tissot, A. & Boillot, M. L. (2012). *Acta Phys. Pol. A*, **121**, 332–335.
- Marcouillé, O., Abualrob, H. B., Brunelle, P., Chapuis, L., Couprie, M.-E., El Ajjouri, T. K., Labat, M., Marlats, J. L., Marteau, F., Mary, A., Nadj, A., Tavakoli, K., Tordeux, M.-A. & Valléau, M. (2014). *Proceedings of the 2014 International Particle Accelerator Conference*, Dresden, Germany, pp. 1998–2000.
- Meller, R. E., Chao, A. W., Peterson, J. M., Peggs, S. G. & Furman, M. (1987). Report SSC-N-360.
- Nadji, A., Chubar, O., Idir, M., Level, M.-P., Loulergue, A., Moreno, T., Nadolski, L. & Polack, F. (2004). *Proceedings of the 2004 European Particle Accelerator Conference*, Lucerne, Switzerland, pp. 2332–2334.
- Nadolski, L., Benabderrahmane, C., Betinelli-Deck, P., Bouvet, F., Brunelle, P., Buteau, A., Cassinari, L., Couprie, M.-E., Delétoille, X., Herbeaux, C., Hubert, N., Labat, M., Lamarre, J.-F., Lebasque, P., Lestrade, A., Loulergue, A., Marchand, P., Marcouillé, O., Marlats, J. L., Nadj, A., Nagaoka, R., Prigent, P., Ricaud, J. P. & Tordeux, M.-A. (2014). *Proceedings of the 2014 International Particle Accelerator Conference*, Dresden, Germany, pp. 200–202.
- Prazeres, R., Ortega, J. M., Bazin, C., Bergher, M., Billardon, M., Couprie, M. E., Velghe, M. & Petroff, Y. (1988). *Nucl. Instrum. Methods Phys. Res. A*, **272**, 68–72.
- Prigent, P., Couprie, M.-E., Hollander, Ph., Labat, M., Laulhé, C., Lestrade, A., Lüning, J., Marlats, J. L., Morin, P., Nadj, A., Ravy, S., Ricaud, J. P., Silly, M. G., Sirotti, F., Tordeux, M.-A. & Zerbib, D. (2014). *Proceedings of the 2014 International Particle Accelerator Conference*, Dresden, Germany, pp. 2059–2061.
- Reiche, S. (1999). *Nucl. Instrum. Methods Phys. Res. A*, **429**, 243–248.
- Schoenlein, R. W., Chattopadhyay, S., Chong, H. H., Glover, T. E., Heimann, P. A., Shank, C. V., Zholents, A. A. & Zolotorev, M. S. (2000). *Science*, **287**, 2237–2240.
- Shimada, M., Katoh, M., Kimura, S., Mochihashi, A., Hosaka, M., Takashima, Y., Hara, T. & Takahashi, T. (2007). *Jpn. J. Appl. Phys.* **46**, 7939–7944.
- Shintake, T. *et al.* (2008). *Nat. Photon.* **9**, 555–559.
- Silly, M. G., Ferté, T., Tordeux, M. A., Pierucci, D., Beaulieu, N., Chauvet, C., Pressacco, F., Sirotti, F., Popescu, H., Lopez-Flores, V., Tortarolo, M., Sacchi, M., Jaouen, N., Hollander, P., Ricaud, J. P., Bergéard, N., Boeglin, C., Tudu, B., Delaunay, R., Luning, J., Malinowski, G., Hehn, M., Baumier, C., Fortuna, F., Krizmancic, D., Stebel, L., Sergo, R. & Cautero, G. (2017). *J. Synchrotron Rad.* **24**, 886–897.
- Streun, A. (2010). SLS Internal Report SLS-TME-TA-2010-0320. Swiss Light Source, PSI, Switzerland.
- Terebilo, A. (2001). SLAC-PUB-8732. SLAC, Stanford University, Stanford, CA, USA.
- Tordeux, M. *et al.* (2012). *Proceedings of the 2012 International Particle Accelerator Conference*, New Orleans, USA, pp. 1068–1070.
- Wiedemann, H. (1993). *Particle Accelerator Physics*. Berlin: Springer.
- Zholents, A. A., Heimann, P., Zolotorev, M. & Byrd, J. (1999). *Nucl. Instrum. Methods Phys. Res. A*, **425**, 385–389.
- Zholents, A. A. & Holldack, K. (2006). *Proceedings of the 2006 Free-Electron Laser Conference*, Berlin, Germany, pp. 725–727.
- Zholents, A. A. & Zolotorev, M. S. (1996). *Phys. Rev. Lett.* **76**, 912–915.